

Improved targeting accuracy of lung tumor biopsies with scanning-beam digital x-ray tomosynthesis image guidance

Geoff Nelson,^{a)} Meng Wu, and Cameron Hinkel
Department of Radiology, Stanford University, Stanford, California 94305

Ganesh Krishna
Palo Alto Medical Foundation, Department of Medicine, University of California San Francisco, San Francisco, California 94143

Tobias Funk
Triple Ring Technologies, Inc., Newark, California 94560

Jarrett Rosenberg and Rebecca Fahrig
Department of Radiology, Stanford University, Stanford, California 94305

(Received 15 April 2016; revised 2 September 2016; accepted for publication 8 October 2016; published 2 November 2016)

Purpose: Electromagnetic navigation bronchoscopy (ENB) provides improved targeting accuracy during transbronchial biopsies of suspicious nodules. The greatest weakness of ENB-based guidance is the registration divergence that exists between the planning CT, acquired days or weeks before the intervention, and the patient on the table on the day of the intervention. Augmenting ENB guidance with real-time tomosynthesis imaging during the intervention could mitigate the divergence and further improve the yield of ENB-guided transbronchial biopsies. The real-time tomosynthesis prototype, the scanning-beam digital x-ray (SBDX) system, does not currently display images reconstructed by the iterative algorithm that was developed for this lung imaging application. A protocol using fiducial markers was therefore implemented to permit evaluation of potential improvements that would be provided by the SBDX system in a clinical setting.

Methods: Ten 7 mm lesions (5 per side) were injected into the periphery of each of four preserved pig lungs. The lungs were then placed in a vacuum chamber that permitted simulation of realistic motion and deformation due to breathing. Standard clinical CT scans of the pig lung phantoms were acquired and reconstructed with isotropic resolution of 0.625 mm. Standard ENB-guided biopsy procedures including target identification, path planning, CT-to-lung registration and navigation to the lesion were carried out, and a fiducial marker was placed at the location at which a biopsy would have been acquired. The channel-to-target distance provided by the ENB system prior to fiducial placement was noted. The lung phantoms were then imaged using the SBDX system, and using high-resolution conebeam CT. The distance between the fiducial marker tip and the lesion was measured in SBDX images and in the gold-standard conebeam-CT images. The channel-to-target divergence predicted by the ENB system and measured in the SBDX images was compared to the gold standard to determine if improved targeting accuracy could be achieved using SBDX image guidance.

Results: As expected, the ENB system showed poorer targeting accuracy for small peripheral nodules. Only 20 nodules of the 40 injected could be adequately reached using ENB guidance alone. The SBDX system was capable of visualizing these small lesions, and measured fiducial-to-target distances on SBDX agreed well with measurements in gold-standard conebeam-CT images ($p = 0.0001$). The correlation between gold-standard conebeam-CT distances and predicted fiducial-to-target distances provided by the ENB system was poor ($p = 0.72$), primarily due to inaccurate ENB CT-to-body registration and movement due to breathing.

Conclusions: The SBDX system permits visualization of small lung nodules, as well as accurate measurement of channel-to-target distances. Combined use of ENB with SBDX real-time image guidance could improve accuracy and yield of biopsies, particularly of those lesions located in the periphery of the lung. © 2016 American Association of Physicists in Medicine. [<http://dx.doi.org/10.1118/1.4966025>]

Key words: medical imaging, image guidance, tomosynthesis, biopsy, lung

1. INTRODUCTION

As improved methods of screening for cancer are being implemented, suspect lesions are being found at earlier stages

and in larger quantities.^{1,2} As a result there is an increase in biopsies, which can be a difficult task in the lungs.³ Methods for lung tumor biopsies have been discussed extensively in the literature.⁴⁻¹¹ A method which poses the fewest

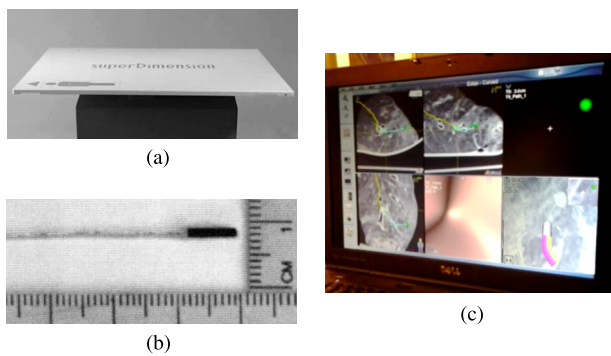


FIG. 1. (a) The ENB coil array which is placed under the patient. (b) The probe used in the working channel. (c) The ENB display during navigation to a lesion.

complication rates for patients is a transbronchial needle biopsy (TBNbx).^{12–14} This approach often uses electromagnetic navigation bronchoscopy (ENB) to help the pulmonologist navigate to the lesion.^{15–19} This method has limitations. While ENB can increase the sensitivity of traditional bronchoscopy in peripheral regions from 14% to somewhere between 59% and 74%, this success rate was correlated with lesion size.^{20–23} It could be improved for small lesions with image guidance.²⁴ An additional limitation is that in order to acquire the biopsy, the probe (see Fig. 1) must be removed from the working channel before the biopsy needle can be inserted. So during the actual biopsy, the pulmonologist is “blind” and has to rely on c-arm fluoroscopy for the ability to “see” what is occurring. Fluoroscopy is very limited in its utility in this process. It is unable to resolve the lesions and only allows the ribs and the pulmonologist’s tools to be seen. One center reported that the diagnostic yield was significantly affected by the CT-to-body divergence.²⁵ Adding real-time image guidance capable of visualizing the lesion would mitigate these limitations.

The scanning-beam digital x-ray (SBDX) system has been proposed as a modality which would facilitate soft tissue visualization during this process.¹⁹ Algorithms have been created for a different SBDX system (one which is optimized for cardiac imaging) which track fiducials or catheters and determine their 3D position.^{26–28} This lung application differs because a small soft-tissue is the focus rather than a metal object which is much easier to resolve. Additionally, the SBDX system used for these experiments has been adapted specifically for this purpose. The distance from the source to the detector is 100 cm and the detector area is 10.7×5.4 cm. The system has an inverse geometry; in the source, the electron beam is scanned over a thin transmission anode. The source is immediately collimated such that the only x-rays which are emitted are in tiny beamlets with a solid angle just large enough for covering the small, photon-counting detector [see Fig. 2(a)]. Because the beamlets are each coming from different angles, tomosynthetic images can be reconstructed. This then reconstructs coronal slices which allow for the visualization of small lesions in the lung.

In this study, the ability of the SBDX system to resolve lesions and improve the pulmonologists targeting accuracy is evaluated. For the evaluation, pig lung phantoms with lesions

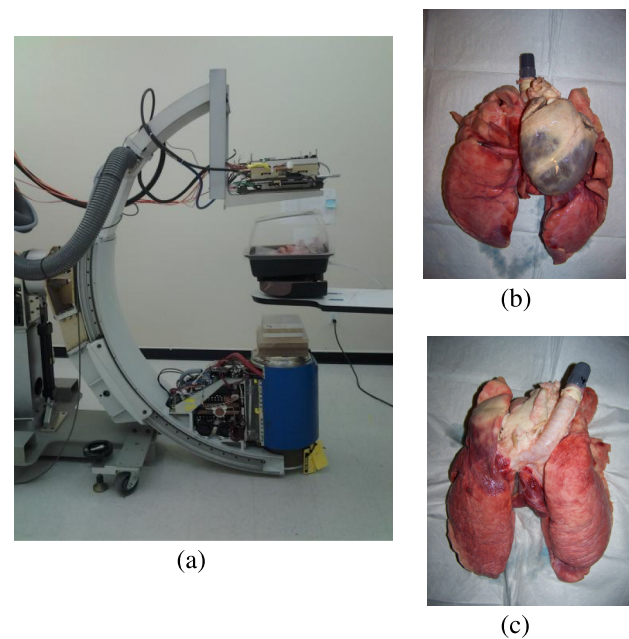


FIG. 2. SBDX system geometry, shown without the anterior portion of the ribs so the lungs are visible (a) and an anterior–posterior and posterior–anterior view of the preserved heart and lungs [(b) and (c)].

are created. Using the ENB system, fiducial markers are placed in the lesions. ENB has been used previously to place fiducials for radiosurgery.²⁹ For our purposes, the fiducials act as place markers indicating where a biopsy would have been taken. After fiducials are placed, they are imaged with the SBDX system and tomosynthetic images are reconstructed. The images are used to determine the shortest distance between the tip of the fiducial and the center of the lesion. An additional CT scan of the lungs is acquired and used as the gold standard for measuring the distance from the tip of the fiducial to the center of the lesion. The CT scan will allow us to evaluate how effective the SBDX image is at accurately showing the lesion to facilitate navigation. It also serves to accurately measure the performance of the ENB system.

2. METHODS

2.A. Phantom preparation

As surrogates for human lungs, four *ex vivo* pig lungs were acquired. The hearts remained attached with the pulmonary vasculature intact (see Fig. 2). The pig lungs were specially ordered from a company (NASCO, 901 Janesville Ave., Fort Atkinson, WI) where they were prepared and soaked in humectin (70% propylene glycol and 30% water). This process allows the lungs to be easily stored and preserved for multiple imaging sessions over several months. One-half-inch PVC pipe was placed in the end of the trachea and rubber bands secured the trachea to the pipe. To provide a complex and realistic detection task, the vessels must be filled with fluid; because of the preservation process, this fluid had to be humectin fluid. Three methods to achieve vessel filling were evaluated including direct injection,

gravity-controlled infusion, and manual pumping. Direct injection was very difficult to implement because the volume of fluid necessary required multiple injections and with each subsequent injection more fluid leaked out. The method which filled the vasculature with the greatest volume was to first super glue (Super Glue Corporation, 9420 Santa Anita Avenue, Rancho Cucamonga, CA) the inferior vena cava closed, and then to connect $\frac{3}{8}$ in. plastic tubing into the superior vena cava again using glue. Humectin was then allowed to gravity flow into the heart and lungs. This method required 4 min to achieve complete filling, but the fluid in the lungs slowly leaked into the lung tissue, such that in less than a day after filling the vasculature, there was little fluid in the vessels and the HU value of the lung tissue had increased by an average of 35 HU. In addition, the air capacity was reduced by the fluid uptake, and thus lung motion was reduced when the lungs were set to ‘breathe’ in the vacuum chamber. The method used for filling the vasculature in this study was to submerge the heart in humectin and manually hand-pump the heart. The valves worked passively and in this manner the vasculature was partially filled. The largest vessels were not full, but all of the vessels in the peripheral regions of the lung including those in the region surrounding the created lesions were filled. The lung vasculature was filled immediately prior to imaging tasks, which allowed a time window of 3 hours to complete the imaging during which lung motion was maintained. Figure 3 shows a 1.5 cm thick maximum intensity projection (MIP) of the lungs with the vasculature filled. Regardless of the method chosen to fill the vasculature, the fluid eventually perfused into the tissue over three to four hours.

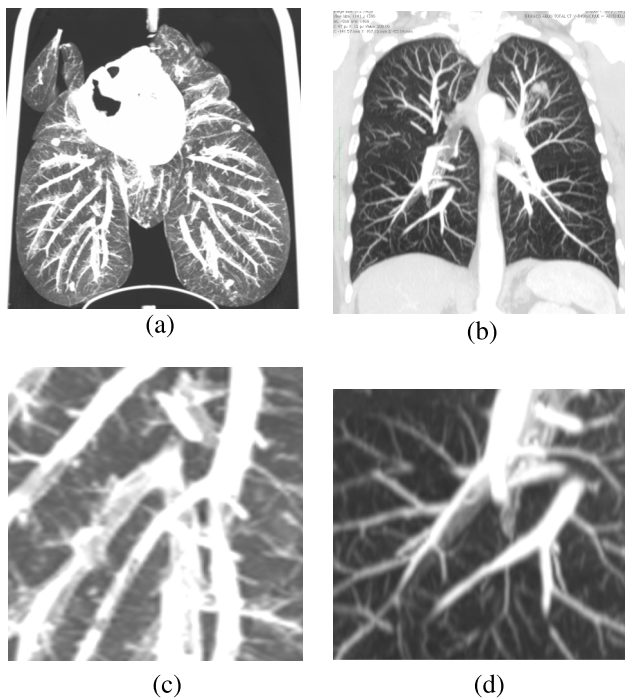


FIG. 3. Images (a) and (b) are 1.5 cm MIPs of the lung phantom with filled vasculature and a patient, respectively. Images (c) and (d) are close-ups of (a) and (b), respectively. The human CT scan is a publicly available data set from OsiriX.

To add lesions to the lungs, a petroleum gel (Summers Labs, Colleagueville, PA) was mixed with Vaseline (Unilever, Blackfriars, London, UK). The Summers labs gel had a very high HU value (~ 2000), while vaseline is ~ 300 HU. A mixture was made to achieve a HU value of approximately -100 , which is in the range of HU values for suspect lung lesions.^{30,31} Note that mixing was carried out at room temperature because if heated to melting, the Summers labs gel formed precipitate and HU values could not be closely controlled. The mixed gel was drawn into a 60 ml syringe, which was then used to backload a 1 ml syringe. The distal regions of the lungs were injected with 0.6 cm^2 of gel per lesion using a 21 ga needle, placed transthoracically at varying depths. Ten such lesions were placed in each lung, with 5 per side [in Fig. 3(a) four lesions are visible].

To inflate the lungs, they were attached to a vacuum chamber and supporting pump. The pump removed the air from the chamber until the lungs were inflated to a pressure of approximately 2 kPa. The PVC pipe in the trachea was connected to an outlet on the vacuum chamber. The pump had timers which enabled the pump to turn off and on cyclically to simulate breathing. Typical change in diameter of a lobe over the course of one breathing cycle was ~ 3 cm.

In order to add ribs to the phantoms, a chest-cavity phantom (custom from the Phantom Laboratory, Salem, NY; water-equivalent plastic surrounding real ribs, sternum and spine) was cut coronally so that the anterior half fits within the vacuum chamber in contact with the lung phantom [see Fig. 8(a)]. The posterior half was placed beneath the vacuum chamber. Thus for fluoroscopy or any anterior–posterior (AP) or posterior–anterior (PA) projection image, with the exception of a difference in magnification of the posterior ribs, the image looks the same as it would for a patient. In the case of tomosynthesis, the posterior portion of the ribs would be more blurred in our phantom because of the additional 4–5 cm between the posterior ribs and the lungs.

2.B. ENB and placement of fiducials

Using a GE Discovery CT750 HD scanner, scans of each lesion-injected lung phantom were acquired with resolution and slice thickness of 0.625 mm as recommended by the ENB system. Path plans were made to navigate to each of the tumor lesions using the standard procedures of the ENB system. For each experiment, a lung phantom was set up and left in the cyclical “breathing” mode. The ENB system attempts to autoregister the planning CT to the probe location in the patient. If the attempt is unsuccessful, the pulmonologist manually registers the CT by navigating to specific bronchial branches and matching them to the CT. In clinical practice, the need to manually register occurs about 25% of the time. The pulmonologist used the normal clinical protocol and procedure for acquiring tumor biopsies with a slight modification. The difference in this experiment from clinical practice was that fiducials were placed at the target tumor location rather than acquiring a tissue sample. Because these lesions had a diameter of 7 mm and were in the peripheral regions of the lungs, the

targeting task was difficult and took significantly longer than navigation takes in a clinical procedure.

The fiducials used were acquired from superDimension (superDimension, Inc., Plymouth, MN). The fiducials were gold (with a minimum purity of 99.99%) and were 0.9 mm in diameter. The double-node fiducials were 13 mm in length; triple-node fiducials were cut into three one-node fiducials, each with a length of 8 mm. These fiducials are no longer used clinically because they were found to migrate *in vivo*. Between imaging sessions, the patient's breathing enables the sharp ends of the fiducial to slowly cut through the lung tissue and move. This is not a problem for our purposes as the lungs do not continue breathing between imaging sessions. Additionally, the preserved lung tissue of our phantoms is slightly tougher than normal lung tissue and so the sharp ends of the fiducial enabled accurate placement. Two other self-coiling fiducials were investigated using C-arm CT imaging prior to and following placement in a nonbreathing lung, and we found that the positions of such soft fiducials could not be guaranteed in our phantom model.

During navigation with the ENB navigation system, the monitor shows the estimated distance from the tip of the probe in the working channel to the center of the target lesion³² (Fig. 1). This channel-to-target distance is an additional aid to the pulmonologist in navigating to the lesion. Because the lesions in this study were so small, the channel-to-target distance was recorded once navigation was completed (before the probe was removed from the working channel and the fiducial was placed). Under fluoroscopic guidance, the pulmonologist inserted the fiducial approximately to the channel-to-lesion distance. This channel-to-target distance was recorded to represent difficulty of fiducial placement and was later compared with the measured fiducial-to-target distances from CT and SBDX. An overview of the steps taken in the measurement process is found in Fig. 4.

2.C. SBDX reconstruction

The most common analytical reconstruction method used for tomosynthesis reconstructions is shift-and-add (SAA).³³ Assuming a parallel-path geometry of the motion of the

tube and/or detector, SAA is performed by shifting each of the projection images by a given amount and then adding them together. By selecting a given shift amount, objects in a given plane are brought into focus. Other SBDX prototypes have utilized multiplane SAA for real-time imaging. Recently, matrix inversion tomosynthesis (MITS) and filtered backprojection (FBP) have received the most attention in the literature.^{34,35} These reconstruction approaches suppress the out-of-plane artifacts using blurring functions on all other planes when a given plane is reconstructed. There is an array of iterative reconstruction algorithms which are currently being investigated for tomosynthesis reconstruction.^{36–38} Iterative reconstruction methods are primarily based upon maximizing the likelihood of Poisson data statistics.³⁹ The iterative reconstruction methods were found to be superior to the FBP for masses and small calcifications for breast tomosynthesis.³⁷

Because the SBDX system has such a low photon count, the data follow Poisson statistics. The system also has low electronic noise. Because of the improved ability to visualize low-contrast objects, an iterative reconstruction algorithm was selected for use with SBDX. Additionally, the iterative technique can better handle potentially low photon counts which may be encountered with thicker patients. The projection data on the SBDX system were acquired at 120 kVp and 15 frame/s with 10 photons per detector pixel on average (the pixel area is 0.44 mm²). The separable quadratic surrogate algorithm was chosen to minimize the cost function.³⁹ The algorithm was stopped after 10 iterations due to the real-time requirement of the system. The resulting reconstruction consisted of a stack of 20 reconstructed planes. The in-plane resolution was 0.5×0.5 mm and the slice spacing was 4 mm with a slice thickness of approximately 4.2 mm.

2.D. Imaging evaluation

Following placement of fiducials in the breathing lung under ENB guidance, CT scans were acquired using a robotic C-arm CT system (Zeego Axiom-Artis, Siemens HealthCare AX, Forchheim, Germany). The reconstructed images had an isotropic voxel size of 0.6914 mm. All reconstructed images

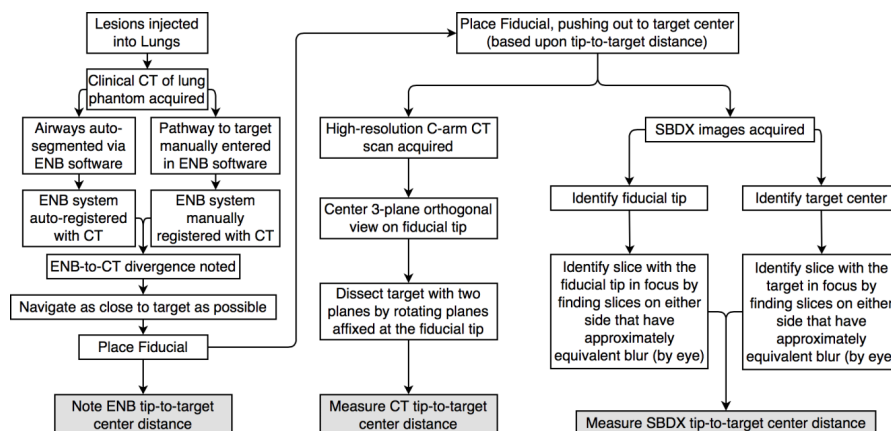


FIG. 4. The steps taken in acquiring measurements across the ENB, CT, and SBDX systems.

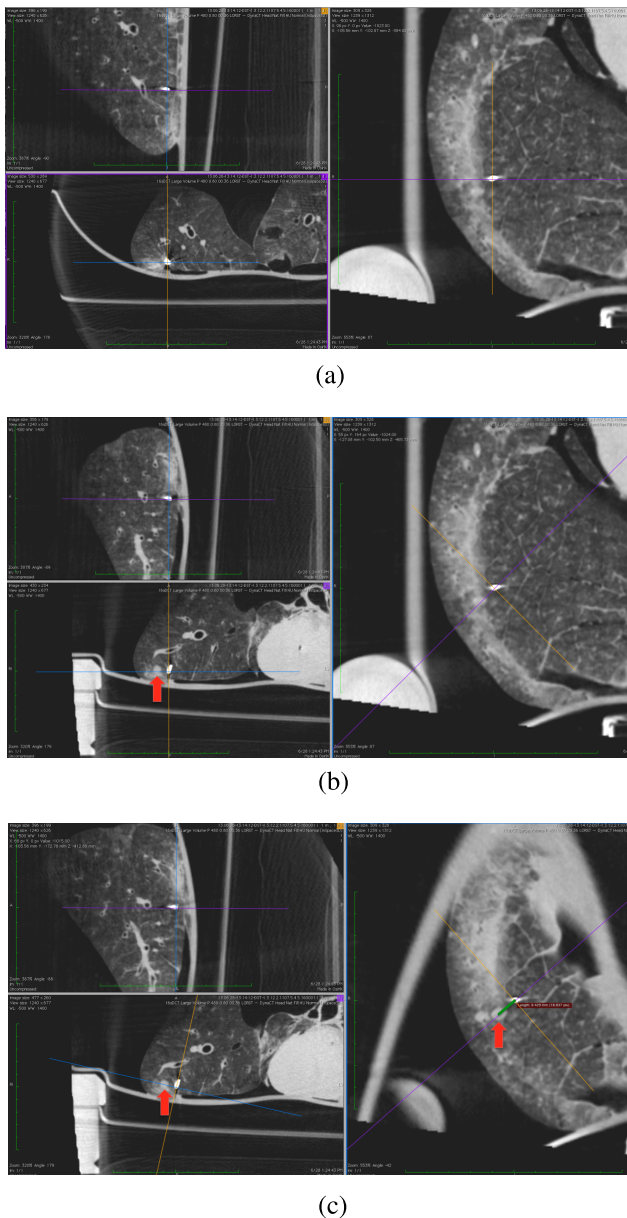


FIG. 5. Steps in measuring the distance from the distal tip of the fiducial to the center of the lesion. (a) All three planes are centered on the distal tip of the fiducial. (b) The right plane is held stationary while the other two are rotated until the bottom left plane bifurcates the lesion. (c) The bottom left plane (with the lesion cross section) was held stationary while the other two were rotated until the right plane also bifurcated the lesion. The distance to the center of the lesion was measured in this view.

were used to measure the distance from the distal tip of the fiducial to the center of the lesion using OsiriX (OsiriX v.5.7 32-bit, Pixmeo SARL Bernex, Switzerland). Three orthogonal planes were centered on the distal tip of the fiducial [Fig. 5(a)]. One plane remained stationary while the other two planes were rotated until the lesion appeared in a plane with the largest area [so the plane approximately dissected it, Fig. 5(b)]. Next, the plane with the cross section of the lesion was held stationary while the other two planes were rotated until the lesion was dissected by one of the two [Fig. 5(c)]. Then the distance from the fiducial tip to the center of the lesion was directly measured. These measurements were used as the gold

standard and compared to the measured distances from the SBDX images. The CT scans were bicubically interpolated and the delineation of the fiducials and lesions was based on this interpolated data.

The ENB channel-to-target distances were acquired at the time of the fiducial placement. The CT scans were acquired for each set of lungs immediately after all fiducials were placed. The lungs were transported to Triple-Ring where they were scanned on the SBDX system. This occurred approximately two weeks after fiducial placement due to limited system availability. This was unlikely to cause fiducial drift because the main cause of drift is breathing and our phantoms were only breathing during fiducial placement and for imaging. For the SBDX scans, the lungs were placed approximately 65 cm from the source. The lungs were moved slightly such that images were acquired with each fiducial near the center of the FOV. The projection data were acquired at 120 kVp and 15 frame/s with 10 photons/pixel on average.

Using these reconstructed images, each with a different fiducial in the center of the FOV, the fiducial-to-target distances on the SBDX were evaluated using ImageJ (NIH, open source software, <http://rsbweb.nih.gov/ij/>). The voxel coordinates were found for the distal tip of the fiducial, as were the coordinates of the center of the lesion which was nearest to the distal fiducial tip. To do this, a stack of reconstructed planes was acquired from the reconstruction. It is not always clear which plane has the distal tip of the fiducial in the best focus. To identify the plane with the fiducial tip, a plane anterior to the tip with some given amount of blur of the tip was visualized (top large square in Fig. 6). Then the plane with the same amount of blur of the tip on the posterior side of the tip was located (bottom large square in Fig. 6). The plane halfway between these two planes is taken as the location of the distal tip of the fiducial (red circle in Fig. 6). This same process was repeated to find the plane with the lesion (blue squares and circle in Fig. 6). Location was assumed to be in the center of the voxel, and the vector distance between the catheter tip and the center of the lesion was calculated using the pixel coordinates and the known voxel size.

3. RESULTS AND DISCUSSION

The fiducial placement task was designed to be difficult for the pulmonologist, so as to present a task where the SBDX system was most likely to have a positive impact on the accuracy of biopsy location. Although lesions of the same diameter (7 mm) are biopsied under ENB guidance when located close to the central branch of the bronchus, lesions in the periphery are not attempted if they are less than 2 cm in diameter. The level of difficulty of the task was evident during placement of fiducials; an average of 7 min was required to navigate to these small peripheral lesions. Typically in clinical settings, navigating to the lesion takes less than one minute. Fifty percent of the lesions were not able to be reached within an appropriate distance to place a fiducial. Additionally about 15% of those lesions were not only beyond an appropriate distance but were not physically

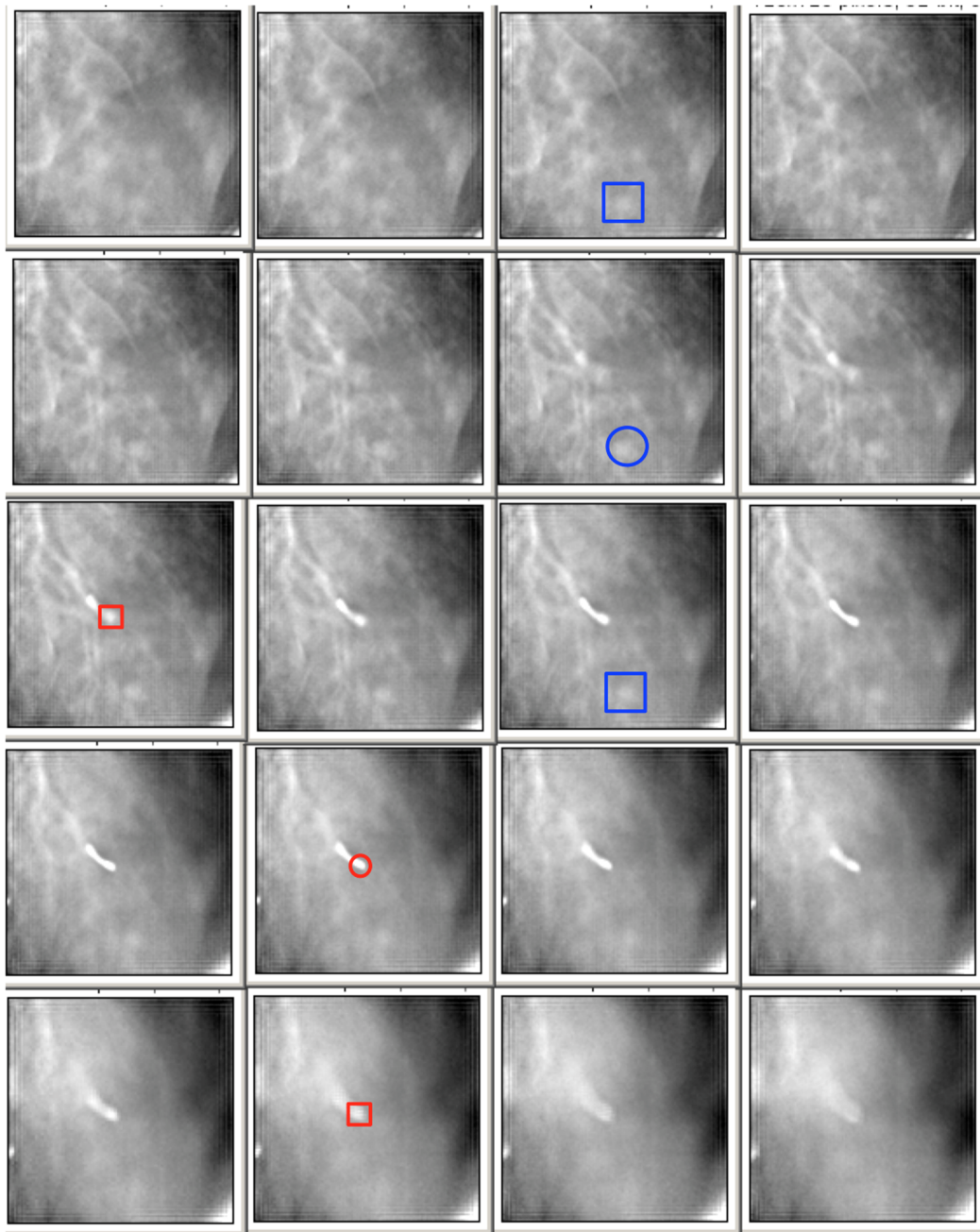


FIG. 6. A set of slices reconstructed at the location of a lesion–fiducial pair. The slice thickness is 4 mm. The large (blue) and small (red) squares represent the distal fiducial tip and lesion, respectively, with a given amount of blur anterior and posterior to the structure location. The circles delineate the structures on the plane in which the structure is assumed to be located/centered.

accessible to the bronchoscope; all such lesions were in the most rostral portions of the upper lobes.

3.A. Imaging evaluation

All of the injected lesions were visible on the SBDX system prior to the placement of the fiducials while none were visible on fluoroscopy. After the placement of the gold fiducials, all but one lesion could be seen on SBDX. The one lesion that could not be seen was obscured by the placed fiducial, which was in the beam path <1 cm from the lesion and could not be sufficiently blurred to resolve the lesion (Fig. 7). At this

time, the modified SBDX gantry we are using cannot easily be rotated, and therefore imaging from oblique angles could not be used to remove the overlap. The SBDX system was able to resolve a lesion even when it was immediately adjacent to the ribs [see Fig. 8(b)].

It is important to note the less-than-ideal condition in which the SBDX system was operated. At the time of the experiment, we were only able to use 71×71 of the source array. This cut our maximum tomographic angle by 20% to 15.9° . We were also unable at the time of the experiment to adjust the mAs, so in order to avoid flooding the detector, we had to add filtration (11 mm Al) to decrease the photon flux,

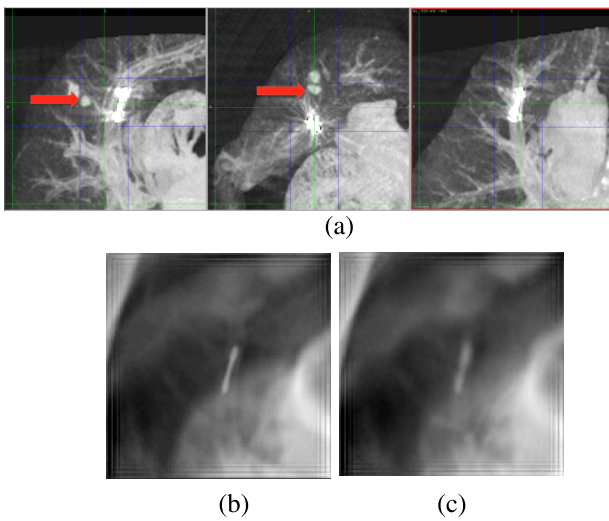


FIG. 7. (a) Sagittal, axial, and coronal MIPs of the lungs, respectively. The dark (blue) lines show the edges of the MIPs in the other two orientations. The arrows show the lesion. (b) The SBDX image of the plane of the fiducial. (c) The SBDX image of the plane of the lesion. Unlike the coronal MIP, the lesion is not visible in the SBDX images. There is not sufficient blurring of the fiducial to resolve the lesion.

which further hardened the beam. Thus the images used in this study are far from ideal conditions and the image quality of an optimized system would be much better than the results presented here.

3.B. Measurement of targeting accuracy

To evaluate the accuracy with which the ENB system and the SBDX system can be used to target the lesion, the fiducial-to-target distances from CT were measured. The fiducial-to-lesion distance as measured in the CT was subtracted from the SBDX fiducial-to-target measurements and ENB channel-to-target measurements. Level of inflation at imaging on SBDX, ENB, and C-arm CT was not identical, leading to small but consistent offsets between the distances measured in each lung (Fig. 9). The concordance correlation coefficient

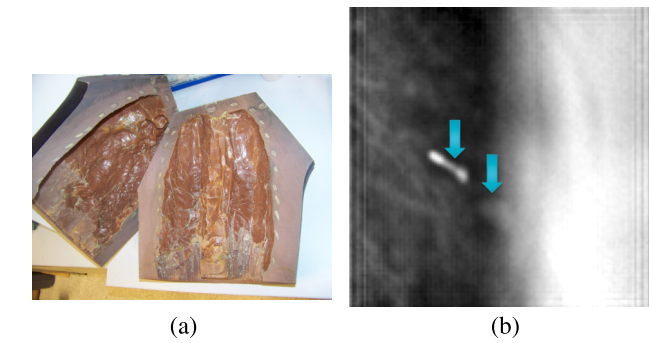
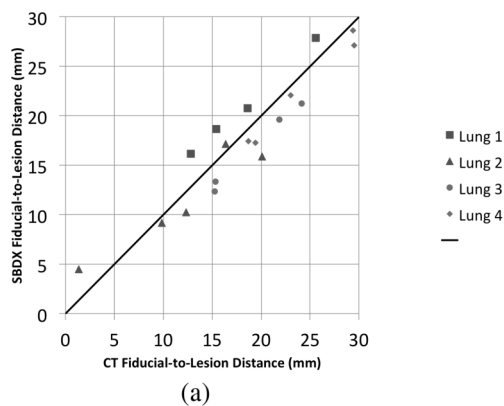


FIG. 8. (a) The coronally cut rib cage phantom. (b) The left arrow points to the two-node fiducial. The right arrow points to the lesion. To the right of the lesion we see the blurred rib cage.

between CT and SBDX fiducial-to-target distances is 0.926 while the concordance correlation coefficient between CT and ENB channel-to-target distances is 0.048. So the SBDX fiducial-to-target distance measurements significantly ($p < 0.0001$) agree with the ground truth as established by CT, while ENB channel-to-target distance measurements show no concordance with the ground truth ($p = 0.72$), which is apparent in Fig. 9 and summarized in Tables I and II.

This study has demonstrated the ability of the SBDX system to visualize small tumor lesions, even in the presence of ribs and filled vasculature. We have also shown that our results match well with the current recommendations given for the ENB system. Tumors in the peripheries must be at least 2 cm in diameter in order to achieve reasonably accurate biopsy samples. As seen in Fig. 9, the pulmonologist would be capable of navigating to within 1.5 cm of the lesions if there was perfect CT-to-body registration and the lungs were not breathing. The CT-to-body divergence as estimated by the ENB system is summarized in Table I. While not significant ($p = 0.10$), we can see that the concordance correlation is improved for the autoregistered lungs. It is possible that a much larger sample size would show that the difference in autoregistered and manually registered lungs is significant. The ENB system is not capable of achieving a registration better than 3 mm,

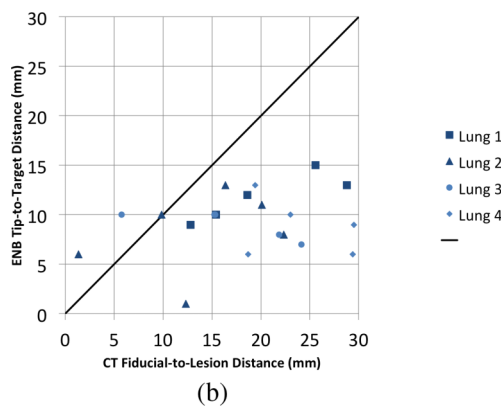


FIG. 9. Graphs comparing the SBDX and ENB measurements to the gold-standard CT measurements. (a) SBDX divergence from CT. Lungs could not always be inflated to the same level, thus there is some offset due to different levels of inflation. (b) ENB divergence from CT. All ENB channel-to-target measurements are less than 1.5 cm. Two measurements from Lung 3 and a measurement from Lung 1 overlap at a CT fiducial-to-target distance of ~15.2 and an ENB channel-to-target distance of 1.

TABLE I. Summary of the ENB-system-generated CT-to-body divergence for each of the four lungs. Also shown are the concordance correlation coefficients for each set of lungs, as well as for the total autoregistered lungs (1 and 2) and the manually registered lungs (3 and 4). A plot of this same data is summarized in Fig. 9(b).

Lung	Divergence (mm)	Concordance	
1	3	0.2014	0.2243
2	4	0.1865	
3	10	-0.137	-0.065
4	8	-0.033	

TABLE II. This shows how much SBDX and ENB distances differ from the gold-standard CT distances.

Variable	N	Mean	Std. Dev.	Min	Max
SBDX measurement error	20	-0.30	2.54	-4.22	4.41
ENB measurement error	20	-11.75	7.10	-24.70	1.15

in part because of the physical limits on the coil array and probe. This problem is exacerbated by lung motion because the CT scan used for planning is obtained during a breath-hold. This suggests that CT-to-body divergence (both from a rigid viewpoint of the primary bronchial passages and from nonrigid breathing deformation) is responsible for the errors in the ENB channel-to-target measurements.

It should also be noted that the inferior portion of the lobes is capable of much more movement in the phantom than is typically seen *in vivo*. This ability of the lungs to move laterally on the inferior portion of the lobes would adversely affect the CT-to-body divergence of the ENB system. Because the lesions in this study were on the peripheries of the lungs, this effect was of particular importance. With the SBDX system on site during the ENB procedure, CT-to-body divergence could be further reduced using tomosynthesis-CT registration.

Future research will place the ENB and SBDX systems together so that a direct comparison of ENB accuracy with and without real-time SBDX guidance can be carried out. The ability to accurately biopsy all lesions (including those not reached under ENB alone in this study) and the SBDX dose per nodule will also be evaluated.

4. CONCLUSIONS

The ENB system greatly facilitates transbronchial biopsies. The greatest weakness of the ENB system is CT-to-body registration divergence. The advantage of the SBDX system over fluoroscopy in visualizing lesions is clear (Fig. 10). The SBDX system is capable of resolving small lesions and could provide real-time 3D image guidance and verification of biopsy location at the time of biopsy. The real-time 3D image guidance can mitigate the problem of CT-to-body divergence. This study suggests that added SBDX imaging will greatly improve targeting for small peripheral lesions and extend the size of lesions and lesion locations for which transbronchial ENB-SBDX-guided biopsy could be used with high accuracy.

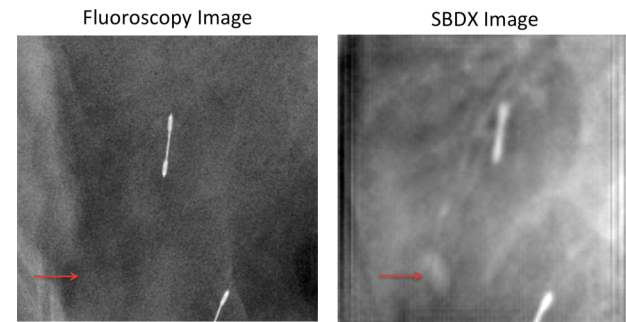


FIG. 10. A fluoroscopy image acquired using the C-arm Zeego system compared to the SBDX system. As seen at the arrows, the small lesion is visible in the SBDX image but not in fluoroscopy.

ACKNOWLEDGMENTS

This work is supported by Grant Nos. NIH R21 HL098683 and NIH S10RR026714-01. The SBDX system was made available by NovaRay, Inc. The vacuum system was made available by Covidien. The authors would like to thank Waldo Hinshaw, Hadley Hicks, and Doug Richter for their helpful discussion and assistance.

CONFLICT OF INTEREST DISCLOSURE

The contributing author Tobias Funk has a conflict of interest as he works for Triple Ring, Inc., which builds the scanning beam digital x-ray system.

^{a)}Author to whom correspondence should be addressed. Electronic mail: geoffsnelson@gmail.com. Banner Radiation Physics - Photon Physics Services.

¹C. I. Henschke, D. I. McCauley, D. F. Yankelevitz, D. P. Naidich, G. McGuinness, O. S. Miettinen, D. M. Libby, M. W. Pasmantier, J. Koizumi, N. K. Altorki, and J. P. Smith, "Early lung cancer action project: Overall design and findings from baseline screening," *Lancet* **354**, 99–105 (1999).

²R. A. Smith, V. Cokkinides, and O. W. Brawley, "Cancer screening in the United States, 2009: A review of current American cancer society guidelines and issues in cancer screening," *Ca-Cancer J. Clin.* **59**, 27–41 (2009).

³S. J. Swensen, J. R. Jett, T. E. Hartman, D. E. Midthun, S. J. Mandrekar, S. L. Hillman, A.-M. Sykes, G. L. Aughenbaugh, A. O. Bungum, and K. L. Allen, "CT screening for lung cancer: Five-year prospective experience," *Radiology* **235**, 259–265 (2005).

⁴R. S. Wiener, L. M. Schwartz, S. Woloshin, and H. G. Welch, "Population-based risk of complications following transthoracic needle lung biopsy of a pulmonary nodule," *Ann. Intern. Med.* **155**, 137–144 (2011).

⁵T. Hiraki, H. Mimura, H. Gobara, K. Shibamoto, D. Inoue, Y. Matsui, and S. Kanazawa, "Incidence of and risk factors for pneumothorax and chest tube placement after CT fluoroscopy-guided percutaneous lung biopsy: Retrospective analysis of the procedures conducted over a 9-year period," *Am. J. Roentgenol.* **194**, 809–814 (2010).

⁶N. Triller, J. Dimitrijevic, and A. Rozman, "A comparative study on endobronchial ultrasound-guided and fluoroscopic-guided transbronchial lung biopsy of peripheral pulmonary lesions," *Respir. Med.* **105**, S74–S77 (2011).

⁷Y. Matsui, T. Hiraki, H. Mimura, H. Gobara, D. Inoue, T. Iishi, S. Toyooka, and S. Kanazawa, "Role of computed tomography fluoroscopy-guided cutting needle biopsy of lung lesions after transbronchial examination resulting in negative diagnosis," *Clin. Lung Cancer* **12**, 51–55 (2011).

⁸S. Gupta, S. Krishnamurthy, L. D. Broemeling, J. Morello, F. A., M. J. Wallace, K. Ahrar, D. C. Madoff, R. Murthy, and M. E. Hicks, "Small (< / =2-cm) subpleural pulmonary lesions: Short- versus long-needle-path CT-guided biopsy-comparison of diagnostic yields and complications," *Radiology* **234**, 631–637 (2005).

- ⁹P. R. Geraghty, S. T. Kee, G. McFarlane, M. K. Razavi, D. Y. Sze, and M. D. Dake, "CT-guided transthoracic needle aspiration biopsy of pulmonary nodules: Needle size and pneumothorax rate," *Radiology* **229**, 475–481 (2003).
- ¹⁰H. Li, P. Boiselle, J. Shepard, B. Trotman-Dickenson, and T. McLoud, "Diagnostic accuracy and safety of CT-guided percutaneous needle aspiration biopsy of the lung: Comparison of small and large pulmonary nodules," *Am. J. Roentgenol.* **167**, 105–109 (1996).
- ¹¹J. S. Klein and M. A. Zarka, "Transthoracic needle biopsy: An overview," *J. Thorac. Imaging* **12**, 232–249 (1997).
- ¹²N. Lechtzin, H. R. Rubin, J. White, P. M. Jenckes, and G. B. Diette, "Patient satisfaction with bronchoscopy," *Am. J. Respir. Crit. Care Med.* **166**, 1326–1331 (2002).
- ¹³E. M. Harrow, W. Abi-Saleh, J. Blum, T. Harkin, S. Gasparini, D. J. Addrizzo-Harris, A. C. Arroliga, G. Wight, and A. C. Mehta, "The utility of transbronchial needle aspiration in the staging of bronchogenic carcinoma," *Am. J. Respir. Crit. Care Med.* **161**, 601–607 (2000).
- ¹⁴P. C. Gay and W. M. Brutinel, "Transbronchial needle aspiration in the practice of bronchoscopy," *Mayo Clin. Proc.* **64**, 158–162 (1989).
- ¹⁵C. R. Dale, D. K. Madtes, V. S. Fan, J. A. Gorden, and D. L. Veenstra, "Navigational bronchoscopy with biopsy versus computed tomography-guided biopsy for the diagnosis of a solitary pulmonary nodule: A cost-consequences analysis," *J. Bronchology Interventional Pulmonol.* **19**, 294–303 (2012).
- ¹⁶K. R. Brownback, F. Quijano, H. E. Latham, and S. Q. Simpson, "Electromagnetic navigational bronchoscopy in the diagnosis of lung lesions," *J. Bronchology Interventional Pulmonol.* **19**, 91–97 (2012).
- ¹⁷B. Lamprecht, P. Porsch, B. Wegleitner, G. Strasser, B. Kaiser, and M. Studnicka, "Electromagnetic navigation bronchoscopy (ENB): Increasing diagnostic yield," *Respir. Med.* **106**, 710–715 (2012).
- ¹⁸R. Bechara, C. Parks, and A. Ernst, "Electromagnetic navigation bronchoscopy," *Future Oncol.* **7**, 31–36 (2011).
- ¹⁹G. Nelson, S. Yoon, G. Krishna, B. Wilfley, and R. Fahrig, "Patient dose simulations for scanning-beam digital x-ray tomosynthesis of the lungs," *Med. Phys.* **40**, 111917 (11pp.) (2013).
- ²⁰Y. Schwarz, J. Greif, H. D. Becker, A. Ernst, and A. Mehta, "Real-time electromagnetic navigation bronchoscopy to peripheral lung lesions using overlaid CT images the first human study," *CHEST J.* **129**, 988–994 (2006).
- ²¹T. R. Gildea, P. J. Mazzone, D. Karnak, M. Meziane, and A. C. Mehta, "Electromagnetic navigation diagnostic bronchoscopy a prospective study," *Am. J. Respir. Crit. Care Med.* **174**, 982–989 (2006).
- ²²R. Eberhardt, D. Anantham, A. Ernst, D. Feller-Kopman, and F. Herth, "Multimodality bronchoscopic diagnosis of peripheral lung lesions a randomized controlled trial," *Am. J. Respir. Crit. Care Med.* **176**, 36–41 (2007).
- ²³R. Eberhardt, D. Anantham, F. Herth, D. Feller-Kopman, and A. Ernst, "Electromagnetic navigation diagnostic bronchoscopy in peripheral lung lesions," *CHEST J.* **131**, 1800–1805 (2007).
- ²⁴J. S. W. Memoli, P. J. Nietert, and G. A. Silvestri, "Meta-analysis of guided bronchoscopy for the evaluation of the pulmonary nodule-guided bronchoscopy for pulmonary nodules," *CHEST J.* **142**, 385–393 (2012).
- ²⁵D. Makris, A. Scherpereel, S. Leroy, B. Bouchindhomme, J.-B. Faivre, J. Remy, P. Ramon, and C.-H. Marquette, "Electromagnetic navigation diagnostic bronchoscopy for small peripheral lung lesions," *Eur. Respir. J.* **29**, 1187–1192 (2007).
- ²⁶M. A. Speidel, M. T. Tomkowiak, A. N. Raval, and M. S. Van Lysel, "Three-dimensional tracking of cardiac catheters using an inverse geometry x-ray fluoroscopy system," *Med. Phys.* **37**, 6377–6389 (2010).
- ²⁷M. A. Speidel, B. P. Wilfley, A. Hsu, and D. Hristov, "Feasibility of low-dose single-view 3D fiducial tracking concurrent with external beam delivery," *Med. Phys.* **39**, 2163–2169 (2012).
- ²⁸C. R. Hatt, M. T. Tomkowiak, D. A. Dunkerley, J. M. Slagowski, T. Funk, A. N. Raval, and M. A. Speidel, "Depth-resolved registration of transesophageal echo to x-ray fluoroscopy using an inverse geometry fluoroscopy system," *Med. Phys.* **42**, 7022–7033 (2015).
- ²⁹D. Anantham, D. Feller-Kopman, L. N. Shanmugham, S. M. Berman, M. M. DeCamp, S. P. Gangadharan, R. Eberhardt, F. Herth, and A. Ernst, "Electromagnetic navigation bronchoscopy-guided fiducial placement for robotic stereotactic radiosurgery of lung tumors a feasibility study," *CHEST J.* **132**, 930–935 (2007).
- ³⁰S. J. Swensen *et al.*, "Lung nodule enhancement at CT: Multicenter study," *Radiology* **214**, 73–80 (2000).
- ³¹Y. Funama, K. Awai, D. Liu, S. Oda, Y. Yanaga, T. Nakaura, K. Kawanaka, M. Shimamura, and Y. Yamashita, "Detection of nodules showing ground-glass opacity in the lungs at low-dose multidetector computed tomography: Phantom and clinical study," *J. Comput. Assisted Tomogr.* **33**, 49–53 (2009).
- ³²S. Leong, H. Ju, H. Marshall, R. Bowman, I. Yang, A.-M. Ree, C. Saxon, and K. M. Fong, "Electromagnetic navigation bronchoscopy: A descriptive analysis," *J. Thorac. Disease* **4**, 173–185 (2012).
- ³³J. T. Dobbins III and D. J. Godfrey, "Digital x-ray tomosynthesis: Current state of the art and clinical potential," *Phys. Med. Biol.* **48**, R65–R106 (2003).
- ³⁴D. J. Godfrey, H. McAdams, and J. T. Dobbins III, "Optimization of the matrix inversion tomosynthesis (MITS) impulse response and modulation transfer function characteristics for chest imaging," *Med. Phys.* **33**, 655–667 (2006).
- ³⁵T. Mertelmeier, J. Orman, W. Haerer, and M. K. Dudam, "Optimizing filtered backprojection reconstruction for a breast tomosynthesis prototype device," *Proc. SPIE* **6142**, 61420F (2006).
- ³⁶Y. Zhang, H.-P. Chan, B. Sahiner, J. Wei, M. M. Goodsitt, L. M. Hadjiiski, J. Ge, and C. Zhou, "A comparative study of limited-angle cone-beam reconstruction methods for breast tomosynthesis," *Med. Phys.* **33**, 3781–3795 (2006).
- ³⁷T. Wu, R. H. Moore, E. A. Rafferty, and D. B. Kopans, "A comparison of reconstruction algorithms for breast tomosynthesis," *Med. Phys.* **31**, 2636–2647 (2004).
- ³⁸J. T. Rakowski and M. J. Dennis, "A comparison of reconstruction algorithms for C-arm mammography tomosynthesis," *Med. Phys.* **33**, 3018–3032 (2006).
- ³⁹J. A. Fessler, "Statistical image reconstruction methods for transmission tomography," *Proc. SPIE* **2**, 1–70 (2000).